

RESEARCH LETTER

Open Access



# Wind tunnel measurements of turbulent boundary layer flows over arrays of ribs and cubes

Ziwei Mo and Chun-Ho Liu\* 

## Abstract

Understanding the effect of building morphology on the flow aloft is important to the ventilation and pollutant removal in cities. This study examines the dynamics over hypothetical urban areas in isothermal conditions using wind tunnel experiments. Different configurations of rib-type and cube-type arrays are designed to model hypothetical rough urban surfaces. The mean and fluctuating velocities are measured by hot-wire anemometry with X-wire probes. The results show that significant variations of fluctuating velocities and momentum fluxes are clearly observed in the near-wall region, depicting the inhomogeneous flow in response to the presence of roughness elements in the lower part of turbulent boundary layer. Comparing the variables over different rough surfaces, the roof-level fluctuating velocities and momentum fluxes increase with increasing surface roughness. Quadrant analyses and frequency spectra collectively suggest that the fresh air entrainment and aged air removal are enhanced over rougher surfaces. Larger energy-carrying turbulence motions contribute mostly to the more efficient ventilation over urban areas.

**Keywords:** Frequency spectra, Momentum fluxes, Quadrant analyses, Turbulent flows, Wind tunnel laboratory experiments

## Background

In the presence of building obstacles in urban areas, the atmospheric boundary layer (ABL) is developed similar to the rough-wall turbulent boundary layer (TBL; Pope 2000). The flow structure and turbulence behavior are highly modified over different types of surface roughness (Jiménez 2004). It is, therefore, important to study the flow characteristics in the TBLs over rough surfaces.

Wind tunnel experiments are commonly performed to examine the turbulent flows over rough surfaces (Rau-pach et al. 1991). Scaling down the dimensions of realistic urban areas in a wind tunnel offers a cost-effective platform for sensitivity tests with full control of variables and boundary conditions (Cermak 1981). A series of wind tunnel studies have been carried out to demystify

the effects of roughness-element configurations on the flows in rough-wall TBLs (Britter and Hanna 2003; Salizzoni et al. 2008; Liu et al. 2015). ABL velocity profiles are examined over arrays of ribs (Salizzoni et al. 2008; Ho and Liu 2017) and arrays of cubes (Cheng and Castro 2002a, b). Some of the aerodynamic parameters, such as displacement height  $d$  and roughness length  $z_0$ , were contrasted over different surface configurations. The effect of roughness elements on the roughness sublayer (RSL) was also investigated (Placidi and Ganapathisubramani 2015). Besides, turbulence structure was characterized by autocorrelation, quadrant analyses as well as spectra over cube-type arrays (Castro et al. 2006). These experimental studies have enriched our understanding of turbulent flows over rough-wall TBLs. However, more wind tunnel results are needed to study the effect of surface configurations on the turbulence behavior and the associated street-level ventilation over urban areas.

\*Correspondence: liuchunho@graduate.hku.hk  
Department of Mechanical Engineering, The University of Hong Kong,  
7/F, Haking Wong Building, Pokfulam Road, Hong Kong, China

In this study, a series of wind tunnel experiments are carried out to examine the flows in the TBLs over rib-type and cube-type arrays. Square aluminum bars and LEGO™ bricks are used to fabricate different configurations of hypothetical urban areas. The profiles of mean wind speeds and turbulence are sampled in each repeating unit of roughness element. The effect of sampling position and rough-surface configurations on the flows is contrasted. Quadrant analyses and frequency spectra are performed as well to elucidate the scale of motions governing the roof-level ventilation mechanism over urban areas.

## Methods

An open-circuit, isothermal wind tunnel, which is located in the Department of Mechanical Engineering, The University of Hong Kong (Ho and Liu 2017; Mo and Liu 2018), is employed to perform the laboratory-scale experiments (Fig. 1a). The dimensions of its test section are 6 m long, 0.56 m wide and 0.56 m high. Repeating units of the reduced-scale models are glued on the whole floor to generate a fully developed TBL (Kozmar 2010). The free-stream wind speed  $U_\infty$  in the wind tunnel is being monitored by a pitot-static tube installed upstream of the test section through a set of experiments to maintain steady wind conditions. The wind tunnel is equipped with a digital traversed system operated by National Instruments (NI 2018) motion control

modules (PCI-7390) for sensor positioning whose spatial resolution is 1 mm in both streamwise  $x$  and vertical  $z$  direction.

## Roughness elements

Models of hypothetical urban areas are fabricated by idealized roughness elements in the wind tunnel test section. Two types of rough surfaces are considered in this study, namely, rib-type arrays and cube-type arrays. The rib-type arrays are assembled by square aluminum bars of size  $l$  ( $=560$  mm; long)  $\times$   $h$  ( $=9$  mm; wide)  $\times$   $h$  ( $=9$  mm; high). The ribs are placed evenly apart in cross-flows, spanning the full width of the wind tunnel test section. Ten configurations of rib-type arrays are adopted by adjusting the separation between the ribs  $w$ . The roughness-element-height-to-separation (aspect) ratios (AR) are equal to 1, 1/2, 1/3, 1/4, 1/5, 1/6, 1/8, 1/10, 1/12, and 1/15. For the cube-type arrays, roughness elements are assembled by staggering LEGO® bricks on a LEGO® baseboard. The size of each piece of LEGO® brick is  $l$  ( $=16$  mm; long)  $\times$   $l$  ( $=16$  mm; wide)  $\times$   $h$  ( $=11.4$  mm; high, including the studs at the top). The separation among the LEGO® bricks is varied in the streamwise  $x$  direction, covering  $h:l$ ,  $h:2l$ ,  $h:3l$ ,  $h:4l$ ,  $h:5l$ ,  $h:6l$ ,  $h:7l$  and  $h:9l$ . In addition, the height of cube-type arrays is increased by mounting double ( $h:4l - D$ ), triple ( $h:4l - T$ ) and quadruple ( $h:4l - Q$ ) layers of LEGO® bricks on the  $h:4l$  configuration. Examples of the roughness configurations (AR = 1/2, AR = 1/4,  $h:2l$ , and  $h:6l$ ) are shown in

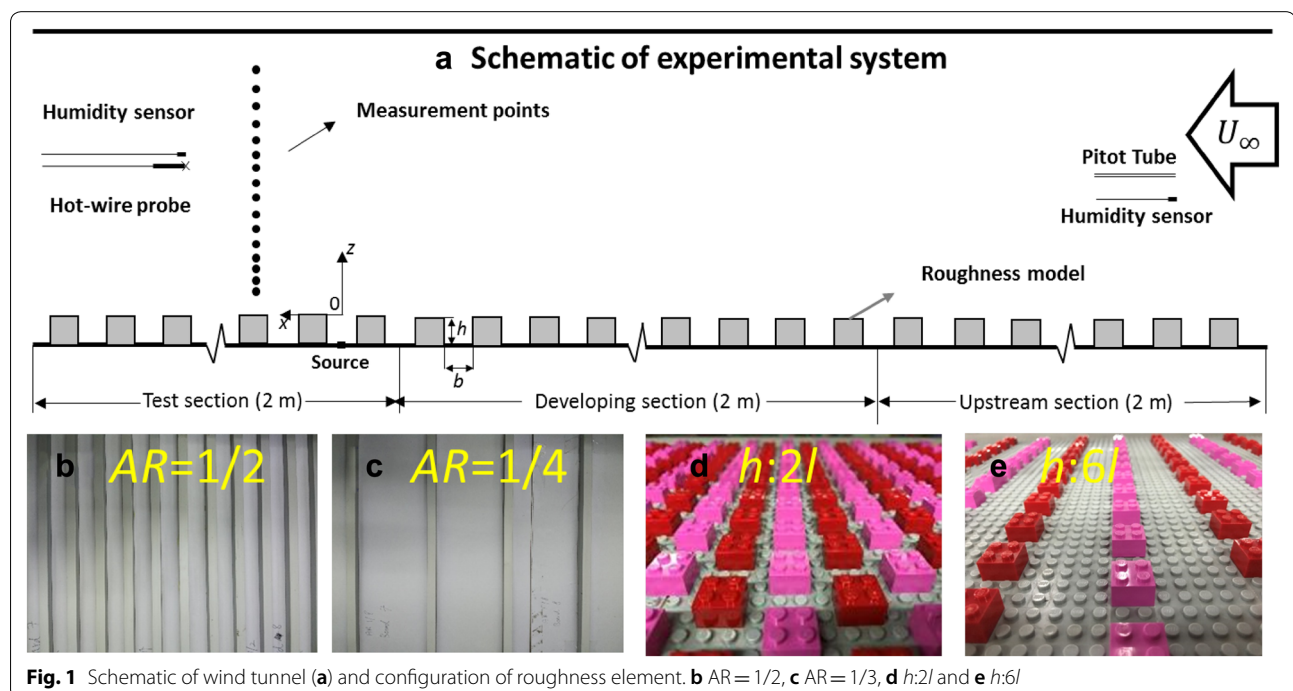


Fig. 1b–e. A total of eleven configurations of cube-type array of roughness element are employed in the wind tunnel measurements.

### Velocity measurements

The mean and fluctuating velocities are measured by a constant-temperature hot-wire anemometer (CTA). A X-wire probe is mounted to measure streamwise  $u$  and vertical  $w$  velocity components. The sensing elements are made of 5- $\mu\text{m}$  (diameter) platinum-plated tungsten wires with 2-mm active length by copper electroplating. The included angle between the two wires is 100° (>90°) that helps reduce the error due to inadequate yaw response in elevated turbulence intensity in near-wall region (Krogstad et al. 1992; Perry et al. 1987; Cheng and Castro 2002a, b). The CTA analog signal is digitized by a 24-bit NI data acquisition module (NI 9239) mounted in a NI CompactDAQ chassis (NI cDAQ-9188). The digital data are then collected by LabVIEW software on a digital computer. The (voltage) signal is then converted to velocity based on the universal calibration scheme (Bruun 1971). The CTA-measured velocity is compared with the velocity measured by the (upstream) pitot-static tube in which the regression coefficient  $R^2$  is up to 0.999. Seven vertical profiles are collected for each repeating unit of roughness element (Fig. 2), covering the top of roughness elements (P1 and P7), cavity top (P3, P4, and P5), leeward edge (P2), and windward edge (P6). A total of 96 sampling points are probed in each vertical profile, ranging from the roughness element height  $z=h$  to the wall-normal distance over the TBLs  $z=350$  mm. The sampling time is 66 s at each point and the sampling frequency is 2000 Hz. Over  $2^{17}$  data are collected at each point and the sampling duration for each case of array configuration is over 12 h.

### Results and discussion

Dynamics over different rough surfaces are analyzed based on the wind tunnel measurements. In the following section, overbar  $\bar{\bullet}$ , angle bracket  $\langle \bullet \rangle$  and double prime  $\bullet''$  ( $=\bullet - \langle \bullet \rangle$ ) denote the temporal average, spatial average and fluctuating component, respectively. Temporal average  $\bar{\bullet}$  is the averaged property during the sampling duration at each point while spatial average  $\langle \bullet \rangle$  is the averaged property at wall-normal distance  $z$  of seven vertical profiles measured at different streamwise positions  $x$ .

### Turbulent boundary layer parameters

Based on the velocity measurements, the TBL parameters in this study are tabulated in Table 1. The TBL thickness  $\delta$  is defined by at the wall-normal distance  $z$  where the spatio-temporal average of mean wind speeds converge to 99% of the free-stream one

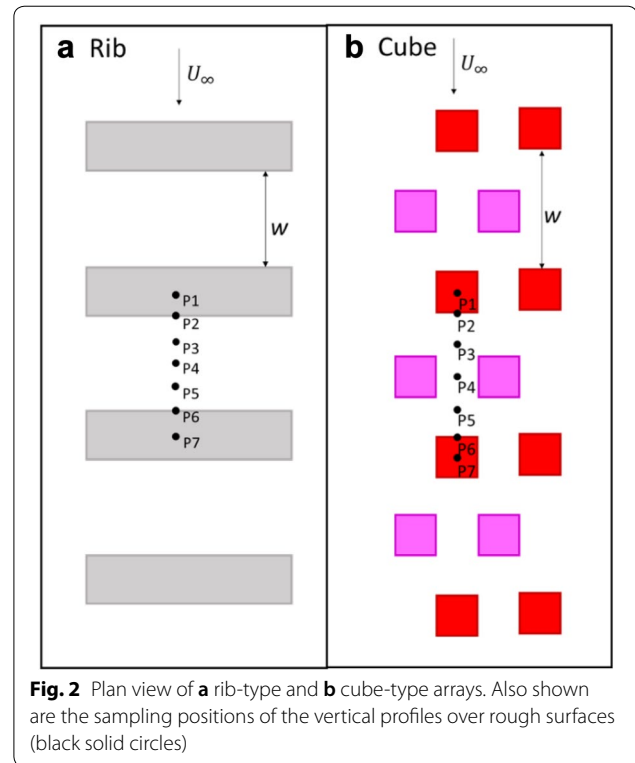


**Fig. 2** Plan view of **a** rib-type and **b** cube-type arrays. Also shown are the sampling positions of the vertical profiles over rough surfaces (black solid circles)

$\langle \bar{u} \rangle|_{z=\delta} = 0.99U_\infty$  (Cheng and Castro 2002a, b). In this study, the free-stream wind speeds at the TBL top are in the ranges of 8–9  $\text{m s}^{-1}$  and 10–11  $\text{m s}^{-1}$ , respectively, for the rib-type and cube-type arrays. The TBL thickness over rib-type arrays is in the range of 219 mm ( $12h$ )  $\leq \delta \leq 304$  mm ( $16h$ ) that is larger than its cube-type counterpart which is in the range of 135 mm ( $5h$ )  $\leq \delta \leq 219$  mm ( $14h$ ). The thicker TBLs over rib-type arrays are caused by the higher obstacle height together with the elevated aerodynamic resistance. The Reynolds number based on free-stream wind speed and TBL thickness  $Re_\infty (=U_\infty\delta/\nu)$  is in the range of  $125,000 \leq Re_\infty \leq 277,000$  for rib-type arrays and  $135,000 \leq Re_\infty \leq 255,000$  for cube-type arrays that is sufficiently high to neglect the effect of molecular viscosity in the analyses.

The friction velocity is defined as  $u_* = (\tau_w/\rho)^{1/2}$  where  $\tau_w$  is the total shear stress on the rough surface and  $\rho$  the fluid density. In the wind tunnel measurements, the friction velocity is commonly estimated by the relationship  $u_* = (\langle u''w'' \rangle)^{1/2}$  by averaging the turbulent momentum flux over the entire rough surface (Cheng and Castro 2002a; Salizzoni et al. 2008). Cheng et al. (2007) reported that  $u_*$  was underestimated by 25% over staggered arrays of cubical elements based on averaging  $\overline{u''w''}$  in the inertia sublayer (ISL) compared with that of direct drag measurement. In addition,  $u_*$  is

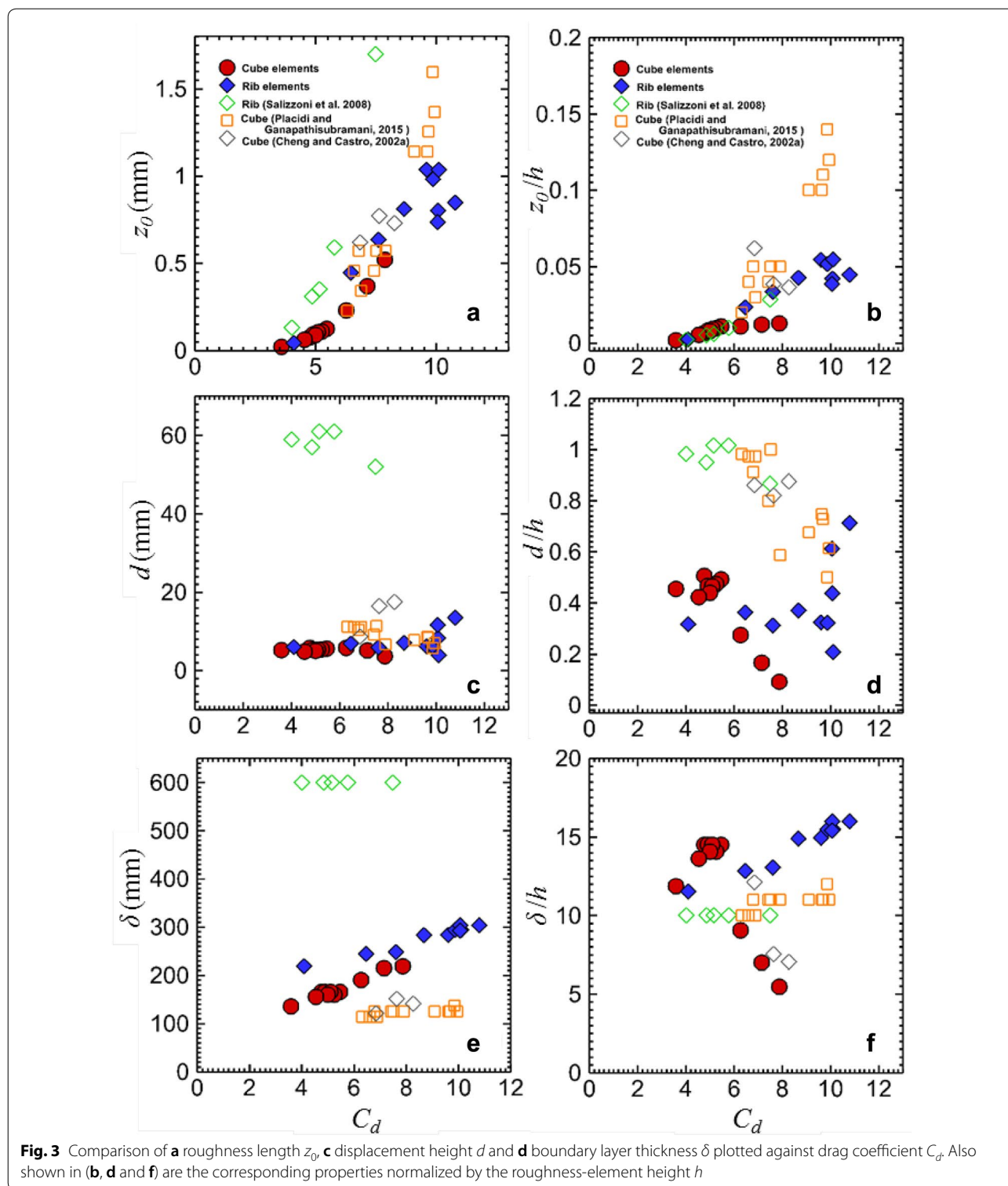
**Table 1** Parameters in the turbulent boundary layers over different rough surfaces

Rough surfaces	$h$ ( $\times 10^{-3}$ m)	$w$ ( $\times 10^{-3}$ m)	$\delta$ ( $\times 10^{-3}$ m)	$U_\infty$ ( $\text{m s}^{-1}$ )	$u_*$ ( $\text{m s}^{-1}$ )	$C_d$ ( $\times 10^{-3}$ )	$d$ ( $\times 10^{-3}$ m)	$z_0$ ( $\times 10^{-3}$ m)
Rib-type arrays								
AR=1/1	19	19	219	8.0	0.36	4.1	6.0	0.04
AR=1/2	19	38	244	8.0	0.45	6.5	6.9	0.44
AR=1/3	19	57	248	8.4	0.52	7.6	5.9	0.63
AR=1/4	19	76	283	8.5	0.56	8.7	7.0	0.81
AR=1/5	19	95	284	8.5	0.59	9.6	6.2	1.04
AR=1/6	19	114	294	8.5	0.60	9.9	6.1	0.98
AR=1/8	19	152	294	8.4	0.60	10.1	4.0	1.04
AR=1/10	19	190	304	9.1	0.65	10.1	8.3	0.80
AR=1/12	19	228	304	9.1	0.67	10.8	13.6	0.85
AR=1/15	19	285	293	9.0	0.64	10.1	11.6	0.73
Cube-type arrays								
$h:l$	11.4	16	135	10.0	0.42	3.6	5.2	0.02
$h:2l$	11.4	32	165	10.9	0.53	4.8	5.8	0.08
$h:3l$	11.4	48	165	10.8	0.54	4.9	5.3	0.09
$h:4l$	11.4	64	165	10.8	0.56	5.5	5.6	0.13
$h:5l$	11.4	80	160	10.6	0.54	5.2	5.4	0.11
$h:6l$	11.4	96	165	10.6	0.54	5.1	5.3	0.10
$h:7l$	11.4	112	160	10.6	0.53	5.0	5.0	0.09
$h:9l$	11.4	144	155	10.7	0.51	4.5	4.8	0.06
$h:4l-D$	21	64	190	10.8	0.60	6.3	5.8	0.23
$h:4l-T$	30.6	64	215	11.1	0.66	7.1	5.1	0.37
$h:4l-Q$	40.2	64	219	11.2	0.70	7.9	3.6	0.52

obtained by assuming it to be the maximum of Reynolds shear stresses in the same studies, and comparable with a corrected estimate value defined as  $(1 + 0.25) \times \langle \overline{u''w''} \rangle^{1/2} \Big|_{\text{ISL}}$  (Manes et al. 2011; Placidi and Ganapathisubramani 2015; Cheng et al. 2007). In this study, we adopt the conventional method by assuming that  $u_*$  is equal to the peaked  $\langle \overline{u''w''} \rangle^{1/2}$ . Although this would introduce error (within 25% uncertainty) in estimating the value of  $u_*$ , the variation pattern of  $u_*$  in this study will not be significantly affected as a consistent method is used among the testing cases. The friction velocity  $u_*$  over rib-type and cube-type arrays is estimated in the ranges of 0.36–0.67  $\text{m s}^{-1}$  and 0.42–0.70  $\text{m s}^{-1}$ , respectively (Table 1). Using  $u_*$  as the slope, the other two key rough-TBL parameters, roughness length  $z_0$  and displacement height  $d$ , are determined by the best fit of the wind-tunnel-measured mean wind speed profiles to the theoretical logarithmic law of the wall (log law). As shown in Table 1, the displacement height is in the range of 4.1 mm ( $0.2h$ )  $\leq d \leq 13.6$  mm ( $0.72h$ ) over the rib-type arrays and 3.6 mm ( $0.09h$ )  $\leq d \leq 5.8$  mm ( $0.5h$ ) over the cube-type arrays. The roughness length  $z_0$  is much smaller, ranging from 0.04 mm ( $0.002h$ ) to 1.04 mm

( $0.06h$ ) over rib-type arrays and from 0.02 mm ( $0.002h$ ) to 0.52 mm ( $0.013h$ ) over cube-type arrays. Drag coefficient  $C_d$  ( $= 2u_*^2/U_\infty^2$ ) is commonly used to measure the aerodynamic resistance for flows over (non-smooth) solid boundaries. It is found to be  $4.1 \times 10^{-3} \leq C_d \leq 10.1 \times 10^{-3}$  over rib-type arrays and  $3.6 \times 10^{-3} \leq C_d \leq 7.9 \times 10^{-3}$  over cube-type arrays.

The variations of TBL parameters, such as  $\delta$ ,  $z_0$ , and  $d$ , are closely influenced by the configurations of surface roughness. The relationship between TBL parameters and the aspect ratio (rib-type arrays) or packing density (frontal and plan solidities of cube-type arrays) has been evaluated in previous studies (Cheng et al. 2007; Placidi and Ganapathisubramani 2015; Ho and Liu 2017). In this paper, we use the drag coefficient  $C_d$  as the quantitative indicator of different configurations of rough surface. Figure 3 plots  $z_0$ ,  $d$ , and  $\delta$  against  $C_d$  in both dimensional and dimensionless form. The data over ribs and cubes obtained from previous studies (Cheng and Castro 2002a; Salizzoni et al. 2008; Placidi and Ganapathisubramani 2015) are also compared. There is a noticeable trend that the  $z_0$  increases with increasing  $C_d$  (Fig. 3a). However, the increasing rate of  $z_0/h$  for cube-type elements and rib-type elements becomes significantly different. It is thus suggested that the roughness-element height  $h$  is not the



most appropriate characteristic length scale for normalization (Fig. 3b). Displacement height,  $d$ , does not show any obvious increase with increasing  $C_d$  for both rib-type and cube-type elements while its dimensionless form  $d/h$

varies significantly (Fig. 3c, d). It is in turn suggested that  $d$  has insignificant relation with  $C_d$ . It should be noted that there is large uncertainty in the estimate of  $d$  by the best fit of measured mean wind profile to the log law.

The TBL thickness  $\delta$  increases slightly with increasing  $C_d$  that suggests a possible relation between them (Fig. 3e). However, scatters of  $\delta$  scaled by the roughness element height  $h$  are found with increasing  $C_d$  for the cube-type elements so they are two different characteristic length scales (Fig. 3f).

**Velocity profiles**

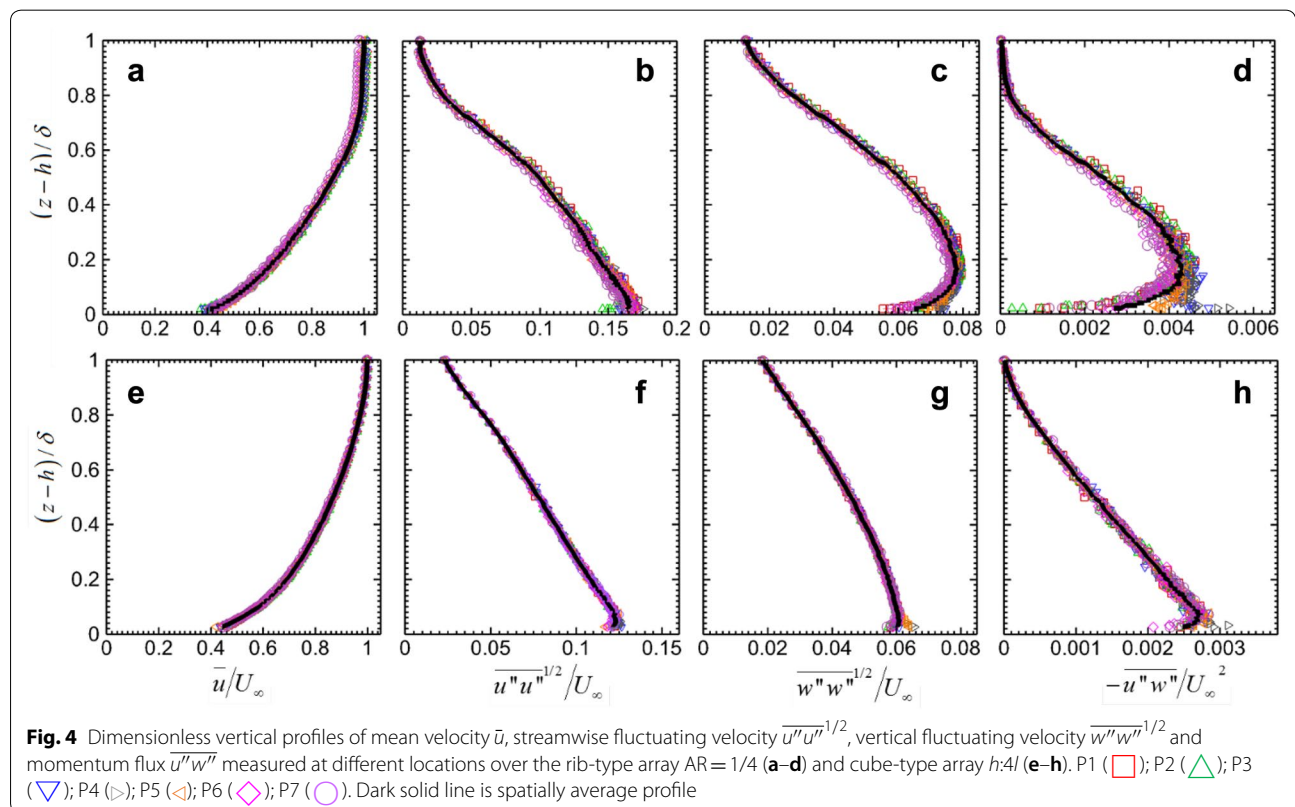
**Velocity profiles measured at different positions**

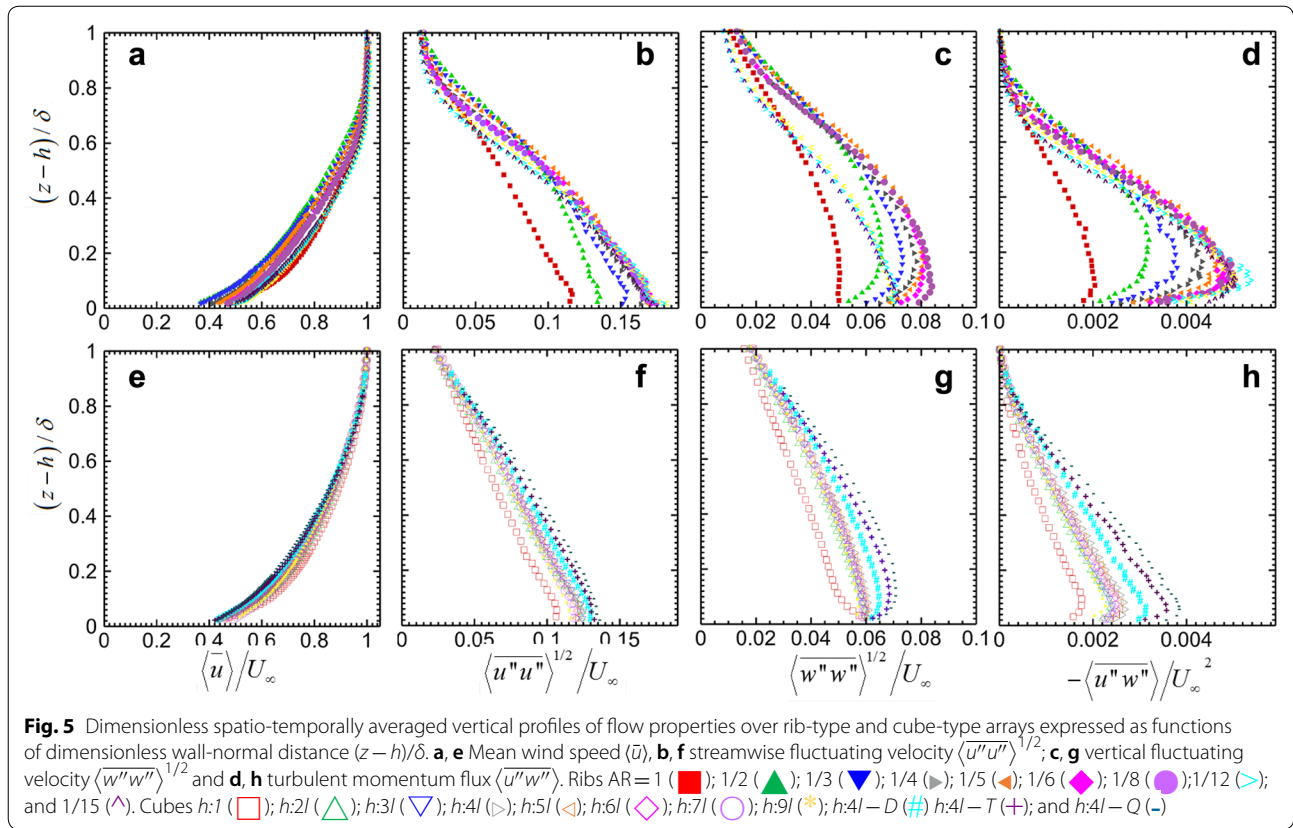
To compare the velocity profiles measured at different positions in a repeating unit of roughness element, Fig. 4 depicts the mean wind speed  $\bar{u}$ , streamwise fluctuating velocity  $\overline{u''u''}^{1/2}$ , vertical fluctuating velocity  $\overline{w''w''}^{1/2}$ , and momentum flux  $\overline{u''w''}^{1/2}$  over rib-type arrays of AR=1/4 and cube-type arrays of  $h:4l$ . The velocities are normalized by the free-stream wind speed  $U_\infty$ . The wall-normal distance is measured from the roof-level  $z-h$  which is then normalized by the TBL thickness  $\delta$ . The gradients of mean wind speed are similar over different measured positions. It is about 40% of  $U_\infty$  at the roughness-element height ( $z=h$ ). The differences of the mean wind speed among individual profiles and their spatial average are less than 6%. However, scattered data (deviations within 12% from the spatially averaged profiles) are found for  $\overline{u''u''}^{1/2}$  and  $\overline{w''w''}^{1/2}$  in the near-wall region ( $z-h < 0.1\delta$ ). It hence, demonstrates the inhomogeneous

flows due to the presence of roughness elements in the lower TBL. This feature is in fact more noticeable for the vertical profiles of  $\overline{u''w''}^{1/2}$ . It highly varies (up to 80% deviation from the spatially average profiles) in the near-wall region, suggesting that significant dynamic effects are induced by individual roughness elements. The inhomogeneous flows are mainly located in  $z-h < 0.1\delta$  over rib-type arrays and even lower in  $z-h < 0.05\delta$  over cube-type arrays. A constant turbulent momentum flux region, which is defined as inertial sublayer (ISL), is revealed in  $0.1\delta < z-h < 0.3\delta$  over rib-type arrays and  $0.05\delta < z-h < 0.15\delta$  over cube-type arrays.

**Velocity profiles measured over different rough surfaces**

To compare the effect of rough-surface configurations on the dynamics, the spatially average profiles of mean wind speed  $\langle \bar{u} \rangle$  (Fig. 5a), streamwise fluctuating velocity  $\langle \overline{u''u''} \rangle^{1/2}$  (Fig. 5b), vertical fluctuating velocity  $\langle \overline{w''w''} \rangle^{1/2}$  (Fig. 5c) and momentum flux  $\langle \overline{u''w''} \rangle^{1/2}$  (Fig. 5d) over an entire repeating unit of roughness element. The mean wind speed profiles are generally similar over different surface configurations, nevertheless, noticeable differences are found in the lower TBL. The roof-level mean wind speeds over all the roughness elements are in the range of  $0.35U_\infty < \langle \bar{u} \rangle_{z=h} < 0.5U_\infty$ .





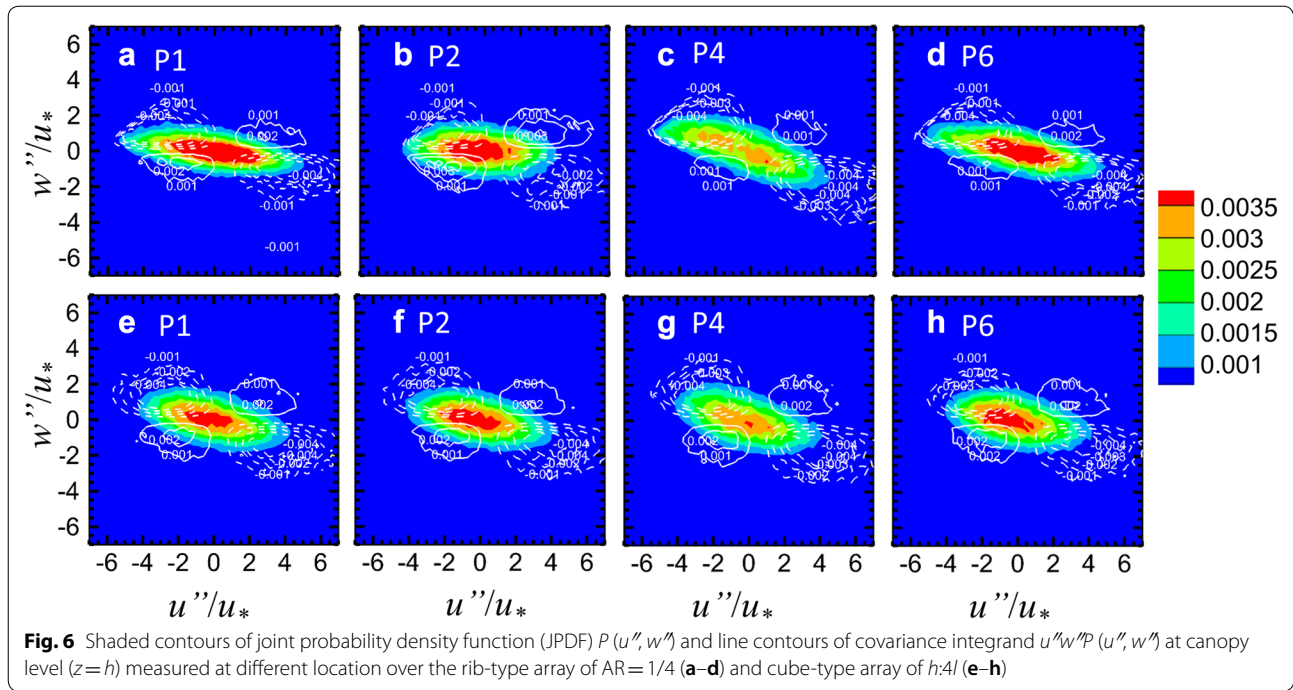
There are notable variations of  $\langle \overline{u''u''} \rangle^{1/2}$ ,  $\langle \overline{w''w''} \rangle^{1/2}$ , and  $\langle \overline{u''w''} \rangle^{1/2}$  over rib- and cube-type arrays, implying that the elevated roof-level turbulence intensity is attributed to the shear close to solid boundary. The variation in velocities over different rib- and cube-type arrays vanishes with increasing wall-normal distance. The mean wind speed profiles collapse in the outer TBL ( $z-h > 0.6\delta$ ) where the flows are barely affected by the surface roughness. The maxima of  $\langle \overline{u''u''} \rangle^{1/2}$ ,  $\langle \overline{w''w''} \rangle^{1/2}$  and  $\langle \overline{u''w''} \rangle^{1/2}$  reside in the near-wall region ( $z-h > 0.1\delta$ ) that increase with widening roughness-element separation. They reach a plateau (over the rib-type array of AR=1/8 and the cube-type array of  $h:4l$ ), then decrease thereafter with increasing the separation. It is because in the closely packed configurations (small separation among roughness elements), namely, skimming flow regime (Oke 1988), the flows seldom entrain into the cavity, resulting in a lower turbulence level. With increasing roughness-element separation, the turbulence level is enhanced by the interaction between the prevailing flows and cavity flows. However, with further increasing separation, the surface becomes smoother again as the roughness elements are sparsely

distributed, which results in lower turbulence level. The high turbulence indicated strong shear over the top of roughness element.

### Quadrant analyses

At the roof level, a substantial variation of turbulence level is observed over different sampling positions (Fig. 4) and over different rough-surface configurations (Fig. 5). To elucidate the momentum transfer between the prevailing flows and cavity flows, quadrant analyses are performed for data at the roof-level sampling points ( $z=h$ ). Based on the instantaneously measured components of fluctuating streamwise  $u''$  and vertical  $w''$  velocity, events of momentum flux transport are categorized into four quadrants, namely, outward interaction Q1 ( $u'' > 0$  and  $w'' > 0$ ), ejection Q2 ( $u'' < 0$  and  $w'' > 0$ ), inward interaction Q3 ( $u'' < 0$  and  $w'' < 0$ ) and sweep Q4 ( $u'' > 0$  and  $w'' < 0$ ) (Wallace et al. 1972; Lu and Willmarth 1973; Wallace 2016). The momentum flux can be calculated by:

$$\overline{u''w''} = \int_{-\infty}^{+\infty} u''w''P(u'',w'')du''dw'', \quad (1)$$



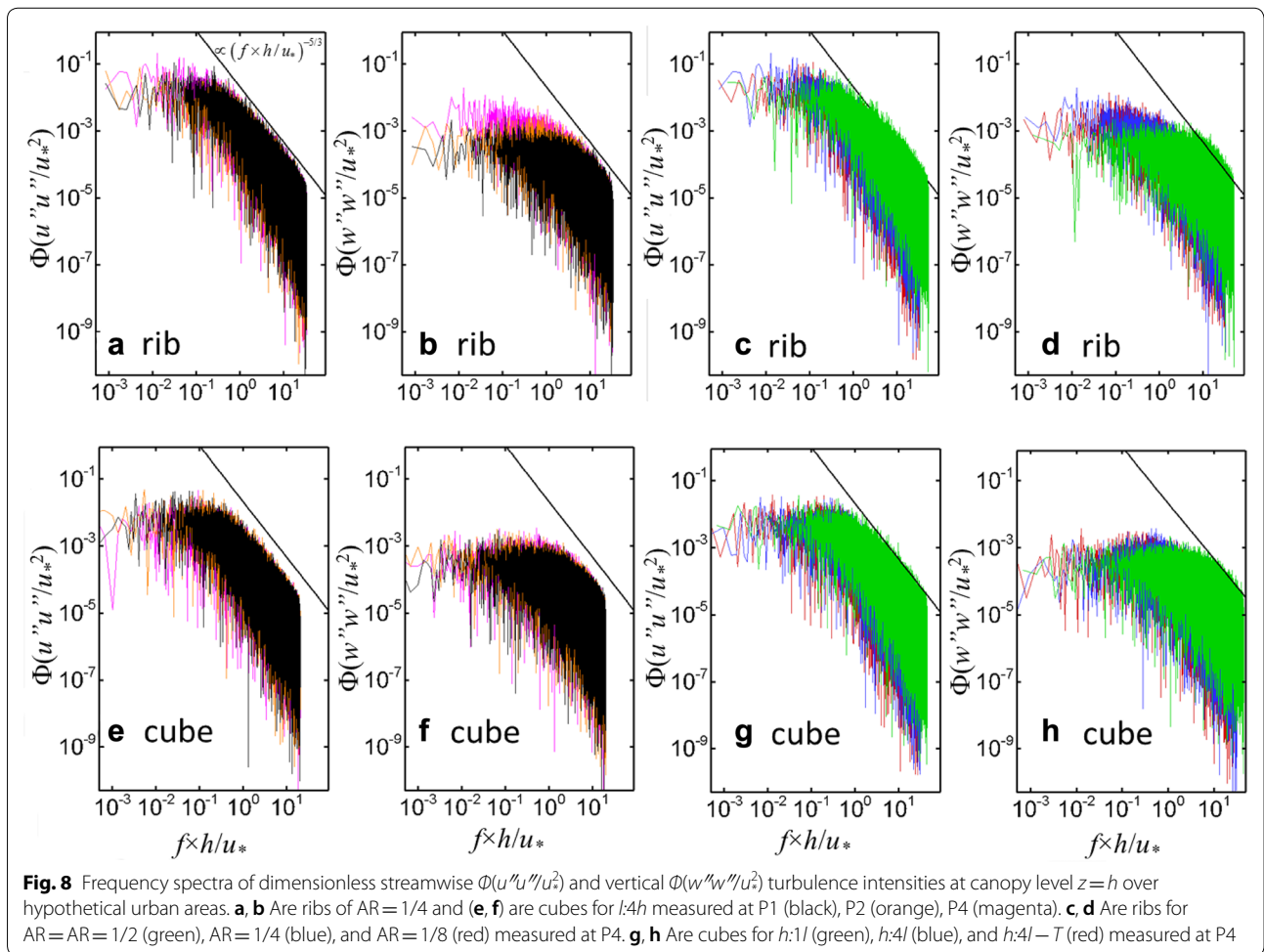
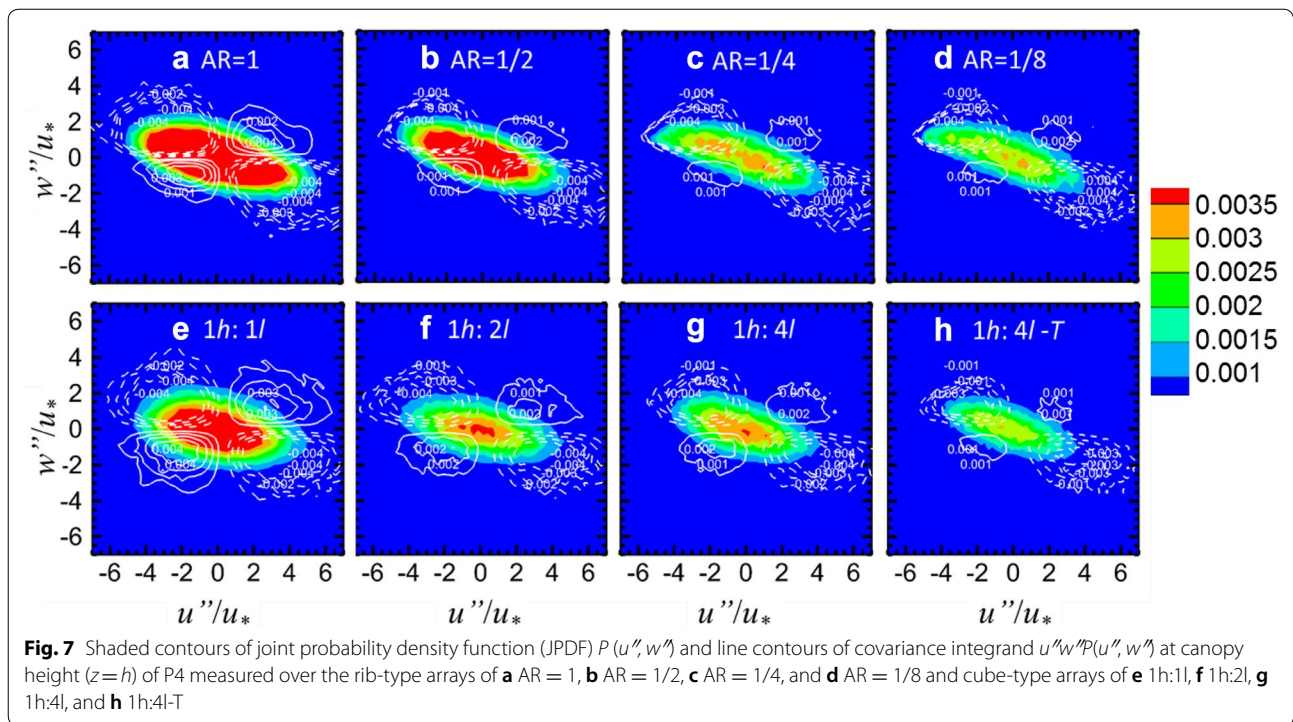
where  $P(u'', w'')$  is the joint probability density function (JPDF) of the fluctuating velocity components  $u''$  and  $w''$ ; here  $u''w''P(u'', w'')$  is the covariance integrand. The JPDF depicts the occurrence frequency of fluctuating velocities  $u''$  and  $w''$  in each quadrant event. The covariance integrand, on the other hand, illustrates the contribution of the total momentum flux to each quadrant. Figure 6 shows the roof-level JPDF and covariance integrand (Fig. 6a over rib-type arrays and Fig. 6e over cube-type arrays), leeward side (Fig. 6b, f), cavity top (Fig. 6c, g), and windward side (Fig. 6d, h). The JPDF is peaked at small fluctuating velocities over roughness elements and on the leeward/windward sides. It spreads out to Q2 and Q4 at cavity top. At the same time, the strength of Q2 and Q4 increases while Q1 and Q3 is suppressed (contour lines). The occurrence of Q2 and Q4 is more frequent than Q1 and Q3, indicating that the ejection Q2 ( $u'' < 0$  and  $w'' > 0$ ) and sweep Q4 ( $u'' > 0$  and  $w'' < 0$ ) dominate the mechanism of roof-level transport processes which is in line with previous studies (Wallace 2016). The larger values of covariance integrand Q2 and Q4 at the cavity top suggest that aged air removal ( $w'' \geq 0$ ) and fresh air entrainment ( $w'' \leq 0$ ) are driven by decelerating ( $u'' \leq 0$ ) and accelerating ( $u'' \geq 0$ ) air masses, respectively.

Figure 7 compares the JPDF and covariance integrand at the cavity top (P4 in Fig. 2) over different rough-surface configurations. It is clearly shown that the JPDF spreads out in the directions of ejection Q2 and sweep Q4 with increasing drag coefficient while Q1 and Q3 are

suppressed accordingly. The covariance integrands of Q2 and Q4 are strengthened with increasing aerodynamic resistance. It is thus suggested that the air entrainment and removal are enhanced over rougher surfaces, resulting in more efficient roof-level ventilation.

### Frequency spectra

Frequency spectra are calculated to examine the roof-level turbulence motion scales (El-Gabry 2014). Similar to the quadrant analyses using the data at cavity top (P4 in Fig. 2), the instantaneous flow signal is proceeded using Fast Fourier Transform (FFT) to convert it from the time domain to the frequency domain (Storey 2002; El-Gabry 2014). As shown in Fig. 8, the energy spectra of  $u''$  are higher than those of  $w''$  over an order of magnitude for  $f \times h/u_* < 1$ , but they decrease sharply when  $f \times h/u_* > 1$  for the streamwise fluctuating velocity  $u''$  and  $f \times h/u_* > 10$  for the vertical fluctuating velocity  $w''$ . The inertial subrange is also clearly depicted for both  $u''$  and  $w''$ , showing the energy cascade in different scales of motions in isothermal conditions. The spectra of  $u''$  and  $w''$  are comparable for  $f \times h/u_* > 10$  because of the isotropic small-scale motions. Comparing the energy spectra over different sampling positions (Fig. 8a, b for rib-type arrays and Fig. 8e, f for cube-type arrays), energy spectra are higher for  $u''$  and  $w''$  at the cavity top (P4) than those at roof level (P1). Large-scale motions enhance the turbulent transport at the cavity top. Comparing the energy spectra over different rough surfaces, large-scale



turbulence is found with increasing drag coefficient over rib-type arrays, especially for vertical fluctuating velocity  $w''$  (taking Case AR=1, AR=1/12, and  $h:l, h:4l-D$  for exempling). The feature is mild for cube-type arrays, probably because the drag coefficient is similar among different cubical roughness elements. These results suggest that the vertical transports are governed by larger scale turbulence with increasing drag coefficient in which the momentum transports are enhanced.

## Conclusions

TBLs over rib- and cube-type arrays are developed in the wind tunnel to examine the flow and turbulence characteristics. For the aerodynamic parameters, a notable trend is observed that roughness length  $z_0$  increases with increasing drag coefficient  $C_d$  while displacement height  $d$  varies significantly with increasing  $C_d$ . Significant variations of fluctuating velocities and momentum flux are found in the near-wall region, demonstrating the inhomogeneous flows due to the presence of roughness elements in the bottom of TBL. Comparing the velocities over different rough surfaces, it is found that the spatially averaged fluctuating streamwise velocity  $\langle u''w'' \rangle^{1/2}$ , fluctuating vertical velocity  $\langle w''w'' \rangle^{1/2}$  and momentum flux  $\langle u''w'' \rangle$  in the near-wall region increase with widening separation among roughness elements, reach a plateau (over rib-type array of AR=1/8 and cube-type array of  $h:4l$ ), then finally decrease with further increasing separation between roughness elements. Quadrant analyses and frequency spectra show that the flow entrainment and air removal are enhanced over rougher surfaces. Larger scale motions of turbulence also effectuate roof-level ventilation over urban areas.

### Author contributions

ZM performed the experiments and drafted the manuscript. CHL performed data interpretation and drafted the manuscript. Both authors read and approved the final manuscript.

### Acknowledgements

Not applicable.

### Competing interests

The authors declare that they have no competing interests.

### Availability of data and materials

The data are available from the corresponding author on reasonable request.

### Ethics approval and consent to participate

Not applicable.

### Funding

This study is partly supported by the General Research Fund (GRF) 17210115 of The Hong Kong Research Grants Council (RGC).

## Publisher's Note

Springer Nature remains neutral with regard to jurisdictional claims in published maps and institutional affiliations.

Received: 27 February 2018 Accepted: 18 June 2018

Published online: 26 June 2018

## References

- Britter RE, Hanna SR (2003) Flow and dispersion in urban areas. *Annu Rev Fluid Mech* 35:469–496
- Bruun H (1971) Interpretation of a hot wire signal using a universal calibration law. *J Phys E Sci Instrum* 4:225
- Castro IP, Cheng H, Reynolds R (2006) Turbulence over urban-type roughness: deductions from wind-tunnel measurements. *Bound Layer Meteorol* 118:109–131
- Cermak JE (1981) Wind tunnel design for physical modelling of atmospheric boundary layers. *J Eng Mech Div ASCE* 108:523–642
- Cheng H, Castro IP (2002a) Near wall flow over urban-like roughness. *Bound Layer Meteorol* 104:229–259
- Cheng H, Castro IP (2002b) Near-wall flow development after a step change in surface roughness. *Bound Layer Meteorol* 105:411–432
- Cheng H, Hayden P, Robins AG, Castro IP (2007) Flow over cube arrays of different packing densities. *J Wind Eng Ind Aerodyn* 95:715–740
- El-Gabry LA, Thurman DR, Poinatte PE (2014) Procedure for determining turbulence length scales using hotwire anemometry. Technical Report NASA/TM—2014-218403, NASA Glenn Research Center, Cleveland, OH, United States
- Ho YK, Liu CH (2017) A wind tunnel study of flows over idealised urban surfaces with roughness sublayer corrections. *Theor Appl Climatol* 130(1–2):305–320
- Jiménez J (2004) Turbulent flows over rough walls. *Annu Rev Fluid Mech* 36:173–196
- Kozmar H (2010) Scale effects in wind tunnel modelling of an urban atmospheric boundary layer. *Theor Appl Climatol* 100:153–162
- Krogstad PA, Antonia R, Browne L (1992) Comparison between rough- and smooth-wall turbulent boundary layers. *J Fluid Mech* 245:599–617
- Liu CH, Ng T, Wong CCC (2015) A theory of ventilation estimate over hypothetical urban areas. *J Hazard Mater* 296:9–16
- Lu S, Willmarth W (1973) Measurements of the structure of the Reynolds stress in a turbulent boundary layer. *J Fluid Mech* 60(3):481–511
- Manes C, Poggi D, Ridolfi L (2011) Turbulent boundary layers over permeable walls: scaling and near-wall structure. *J Fluid Mech* 687:141–170
- Mo Z, Liu CH (2018) Wind tunnel measurements of pollutant plume dispersion over hypothetical urban areas. *Build Environ*. 132:357–366
- NI (2018) National Instrument National Instruments, Austin, TX <http://www.ni.com>
- Oke TR (1988) Street design and urban canopy layer climate. *Energy Build* 11:103–113
- Perry AE, Lim KL, Henbest SM (1987) An experimental study of the turbulence structure in smooth- and rough-wall boundary layers. *J Fluid Mech* 177:437–466
- Placidi M, Ganapathisubramani B (2015) Effects of frontal and plan solidities on aerodynamic parameters and the roughness sublayer in turbulent boundary layers. *J Fluid Mech* 782:541–566
- Pope SB (2000) *Turbulent flows*. Cambridge University Press, Cambridge
- Raupach MR, Antonia RA, Rajagopalan S (1991) Rough-wall turbulent boundary layers. *Appl Mech Rev* 44(1):1–25
- Salizzoni P, Soulhac L, Mejean P, Perkins RJ (2008) Influence of a two-scale surface roughness on a neutral turbulent boundary layer. *Bound Layer Meteorol* 127:97–110
- Storey BD (2002) Computing Fourier series and power spectrum with Matlab. TEX paper
- Wallace JM (2016) Quadrant analysis in turbulence research: history and evolution. *Annu Rev Fluid Mech* 48:131–158
- Wallace JM, Brodkey RS, Eckelmann H (1972) The wall region in turbulent shear flow. *J Fluid Mech* 54:39–48